Research Square

Preprints are preliminary reports that have not undergone peer review.
They should not be considered conclusive, used to inform clinical practice,
or referenced by the media as validated information.

Influence of laser beam shaping on process stability, build rate, and microstructure in laser powder bed fusion of AlSi10Mg.

Pierre HEBRARD
Bassem BARKIA
Ali Gokhan Demir
Emilie Le Guen
Leonardo CAPRIO
Morgan DAL
Frédéric COSTE
Patrice Peyre

patrice.peyre@ensam.eu

CNRS: Centre National de la Recherche Scientifique https://orcid.org/0000-0002-3679-9622

Research Article

Keywords: L-PBF, AlSi10Mg alloy, laser beam shaping, porosity, microstructure

Posted Date: November 9th, 2026

DOI: https://doi.org/10.21203/rs.3.rs-11321837/v1

License: This work is licensed under a Creative Commons Attribution 4.0 International License.
Read Full License

Influence of laser beam shaping on process stability, build rate, and microstructure in laser powder bed fusion of $AlSi_{10}Mg$

Pierre Hébrard*, Bassem Barkia*, Ali Gökhan Demir**, Emilie Le Guen***, Léonardo Caprio**, Morgan Dal*, Frédéric Coste* and Patrice Peyre*, [a]

* PIMM, Arts et Métiers, Cnam, CNRS UMR 8006, 151 bd de l'Hôpital, 75013, Paris, France

** Department of Mechanical Engineering, Politecnico di Milano, Via La Masa, 20156, Milan, Italy

*** I2M, UMR 5295 CNRS-Université de Bordeaux, 351 Cours de la Libération, 33405 TALENCE, France

[a] Corresponding author : patrice.peyre@ensam.eu

Abstract

Laser beam shaping offers promising opportunities to stabilize the laser powder bed fusion (L-PBF) process and improve manufacturing performance. However, most previous studies have focused on shaped beams with spot diameters above 0.2 mm, substantially larger than those conventionally used in L-PBF (<0.1 mm). Here, we investigate annular and near-top-hat beam profiles with dimensions close to the conventional range for processing AlSi10Mg, using a Gaussian beam as the reference across different optical arrangements with an interlaboratory approach. At moderate laser powers (300-500 W), beam shaping widens the viable power–scan speed (P, V) processing window by delaying the onset of keyhole formation. Compared with the Gaussian beam, the shaped profiles produce shallower and wider melt pools, characterized by higher width-to-depth ratios, while also improving the surface quality of the fabricated parts, as evidenced by lower average roughness (S_a). Microstructural analysis reveals slightly stronger crystallographic textures for the near-top-hat and annular profiles, whereas the average grain size remains essentially unchanged. Consistently, no clear difference in tensile strength is observed between specimens produced using the near-top-hat and Gaussian profiles. At higher laser power (700 W), the annular beam enables stable processing at scan speeds up to 2.6 m s^{-1}, yielding build rates of approximately 20 mm^3 s^{-1}, about twice those achieved with the Gaussian profile. This productivity gain is attributed to the more stable laser–matter interaction resulting from the lower peak irradiance of the annular intensity distribution. Although the shaped beams generate more spatter, this does not adversely affect the surface roughness of the fabricated parts. These results show that small-sized top-hat, annular, and core/ring beams provide an effective means of extending the stable processing range of L-PBF while improving surface quality and enabling substantially higher build rates.

Keywords

L-PBF, $AlSi_{10}Mg$ alloy, laser beam shaping, porosity, microstructure

1- Introduction

Laser powder bed fusion (L-PBF) of aluminium alloys requires a narrow balance between insufficient melting and excessive vaporization [1]. Conventional single-mode fiber lasers typically produce a near-Gaussian irradiance profile, characterized by a pronounced central intensity peak. This promotes efficient coupling and deep penetration, but it can also intensify recoil-pressure-driven melt-pool depression, keyhole instability, pore formation, and spatter at high energy input [2–4] [3]. Spatter and powder-bed redistribution can in turn disturb subsequent layers and contribute to local lack of fusion [5–7].

Spatial beam shaping offers an additional way to control the laser–material interaction beyond conventional process parameters such as laser power, scan speed, hatch distance, layer thickness, and scan strategy. By changing how the laser energy is distributed across the beam, for example by reducing the central peak or shifting part of the power toward an outer ring, the melt-pool geometry and dynamics can be modified [8, 9]. This can affect melt-pool depth and width, fluid flow, solidification behaviour, and surface stability. Non-Gaussian beam profiles have therefore gained increasing interest for their potential to widen the processing window, improve productivity, and influence microstructural development [10]. However, reliable beam-profile characterization and the transfer of optimized conditions between different machines and optical systems remain important challenges [11].

Beam shaping can be achieved either with fixed optical components, such as diffractive optical elements (DOEs), or directly at the laser source [12, 13]. In-source systems distribute the laser power between a central core and one or more annular regions, allowing rapid switching between Gaussian, near-top-hat, and annular beam profiles. These approaches differ in flexibility, optical efficiency, and sensitivity to the optical configuration. Therefore, the actual irradiance distribution should be measured rather than assumed from the nominal beam profile.

Experimental data on shaped beams remain relatively scarce for aluminium alloys. Loh et al. [14] observed distinct melt-track responses under uniform and Gaussian irradiation. [15] later showed that an annular profile extended the range of power and scan speed yielding high-density AlSi10Mg.Patel et al. [16] found that defocusing a sub-100 µm Gaussian beam favoured conduction-mode melting and reduced keyhole-related defects. For AlSi7Mg0.6 processed with an in-source multicore laser, Galbusera et al. [17] identified peak irradiance and the fraction of power in the outer ring as key parameters controlling melt-pool depth and aspect ratio. Taken together, these studies indicate that redistributing irradiance can reduce excessive penetration in Al–Si alloys. Direct comparison remains difficult, however, because the beam dimensions and optical configurations differ from one study to another.

A further difficulty is that changes in beam profile are often accompanied by changes in spot size, focal position or laser power. The effect of the spatial distribution cannot then be isolated from that of the other variables. Grünewald et al. [13], for example, estimated that the build rate of AISI 316L could be approximately doubled by replacing a 100 µm Gaussian spot operated at 450 W with a 250 µm ring-shaped spot operated at 1.05 kW. Since both power and spot size were increased, the contribution of the ring profile alone is unclear. Most shaped-beam studies have also used spot diameters larger than 0.2 mm, whereas conventional L-PBF commonly uses diameters below 0.1 mm. The distinction matters because spot size can itself influence the final microstructure and properties. In AlSi10Mg, increasing the diameter of a Gaussian beam from 60 to 120 µm was shown to coarsen the microstructure, increase elongation, and reduce yield

strength [18]. Beam profiles should therefore be compared using carefully measured spots of similar dimensions.
Changes in the irradiance distribution may also influence solidification and crystallographic texture through their effect on melt-pool curvature and thermal-gradient orientation. Numerical calculations have predicted variations in columnar and equiaxed growth under elliptical and redistributed profiles [19]. Experiments with larger flat-top beams have produced strongly textured or nearly single-crystalline structures in pure Ni and IN738 [20, 21]. More recently, advanced numerical simulations combined with in situ X-ray radiography related core-to-ring power redistribution to pronounced changes in melt-pool width-to-depth ratio [22]. Whether similar changes occur in aluminium alloys, and whether they translate into measurable differences in texture and tensile behaviour, is still poorly documented.
The literature does not yet separate the effects of beam profile and spot size consistently. Most studies examine only one aspect, such as single-track geometry, density, or microstructure, and do not trace the effects of a measured beam profile across process stability, spatter formation, surface quality, bulk microstructure, mechanical properties, and productivity. It therefore remains unclear whether benefits observed at the single-track scale persist in bulk specimens or support higher build rates without reducing part quality.
This study compares Gaussian, near-top-hat, and annular beam profiles with small, comparable spot sizes in order to underline the main governing beam properties across two open-architecture L-PBF systems with an interlaboratory effort. The profiles are respectively generated using static diffractive optical elements and an in-source dual-core laser. The first laser system was employed to characterize the deposition process whilst the second allowed scaling towards the production of tensile specimen for mechanical characterization. Their measured irradiance distributions are correlated with melt-pool geometry, track stability, spatter behavior, surface topography, part density, tensile properties, crystallographic texture, and build rate. Specifically, the study examines whether reducing peak irradiance delays keyhole formation and whether annular irradiation enables the use of higher laser powers and scan speeds without compromising part density. Overall, this work assesses the potential of small-spot beam shaping to improve both the quality and productivity of AlSi10Mg processing.

2- Material and experimental methods

2.1. Powder

The experiments were conducted using gas-atomized AlSi10Mg powder supplied by SLM Solutions GmbH, with a particle-size range of 20–63 µm. According to the supplier's certificate of analysis, the powder contained 9.8 wt.% Si, 0.35 wt.% Mg, and 0.11 wt.% Fe. The concentrations of the other measured elements, including Cu, Mn, Ni, and Ti, were each below 0.01 wt.%. Before laser powder bed fusion (L-PBF), the powder was dried in an oven at 70 °C for at least 48 h. This treatment was performed to remove adsorbed moisture, improve powder spreading, and reduce the risk of hydrogen-induced porosity.

2.2. L-PBF experiments

The experiments were conducted using two complementary open-architecture L-PBF systems: one located at the PIMM laboratory in France and the other at Politecnico di Milano (PoliMi) in Italy. The PoliMi system provided a larger build volume, enabling the production of larger specimens.

2.2.1. L-PBF experiments with DOEs at PIMM Lab.

The MiMAS system at PIMM, described by [23], was equipped with a 1 kW redPOWER QUBE single-mode fiber laser (SPI Lasers). The system was used to produce rectangular specimens measuring 10 × 10 × 2 mm³ under three beam configurations: a Gaussian shape (G) of 55 µm diameter, an annular shape (A) of 90 µm diameter at $D_{4\sigma}$, and a near-top-hat (T) shape of 65 µm diameter (**Table 1**).

The near-top-hat (T) and annular BS (A) profiles were generated using two dedicated diffractive optical elements (DOEs) positioned downstream of the collimation unit. The resulting spatial intensity distributions were characterized using a Spiricon beam analyzer equipped with an SP928 CCD sensor featuring a resolution of 1928 × 1448 pixels and a pixel pitch of 3.69 µm.

The measured intensity distributions are presented in **Fig. 1** and **Fig. 2*a***. At the focal plane (z = 0 mm), the annular beam exhibited the intended ring-shaped distribution, although a localized region of increased intensity was observed. By contrast, the near-top-hat beam deviated substantially from the target uniform intensity profile and more closely resembled a defocused Gaussian beam. A broad processing window was investigated, with laser powers ranging from 150 to 900 W and scan speeds ranging from 0.5 $m.s^{-1}$ to 3.2 $m.s^{-1}$ (**Table 2**). These experiments were designed to evaluate the effect of the beam shape on:

- Melt-pool geometry and process stability, track dimensions, scan-track stability windows as a function of laser power and scan speed (P, V), spatter formation, as-built surface finish, and build rate.
- Porosity rate and microstructure characteristics.

Unless otherwise specified, the hatch spacing, layer thickness, and interlayer scan-rotation angle were maintained at 150 µm, 50 µm, and 67°, respectively.

Spatter emission was characterized using a high-speed camera positioned at grazing incidence, following a procedure similar to that described by [24, 25]. A field of view of 15 × 12.5 mm² was recorded at a spatial resolution of 1280 × 1024 pixels, a frame rate of 10 kfps, and an exposure time of $1/10^5$ s. A FESH0950 short-pass optical filter, with a cutoff wavelength of 950 nm, was used to suppress radiation at the laser wavelength and preferentially collect thermal radiation emitted by high-temperature metallic spatters. The acquired images were subsequently binarized and processed using a Python routine based on the scikit-image library. Spatter particles were counted over a representative sequence of images. The projected spatter area in each frame was calculated as the total number of white pixels in the binary image.

2.2.2. L-PBF experiments with a double-core laser at PoliMi

Cubic specimens measuring 11 × 11 × 11 mm³ were manufactured at PoliMi using a constant laser power of 350 W. The layer thickness and interlayer scan-rotation angle were maintained at 50 µm and 67°, respectively, consistent with the PIMM experiments. Two hatch spacings, 50 and 150 µm, were investigated (**Table 2**). A 1 kW nLIGHT Corona AFX1000 double-core fiber laser that featured 7 different addressable beam shapes was evaluated. Amongst the available beam shapes the Gaussian BS0 profile and the near-top-hat BS5 profile were employed, following the nomenclature introduced by [26]. Their measured intensity distributions are shown in Fig. 2b.

The relative density, melt-track dimensions, and microstructure, characterized by electron backscatter diffraction (EBSD), were analyzed. This investigation did not include a systematic assessment of the process-stability windows. Tensile specimens were also fabricated using the

scan speeds that yielded the highest densification for each beam profile, enabling the potential influence of beam shaping on mechanical strength to be evaluated.

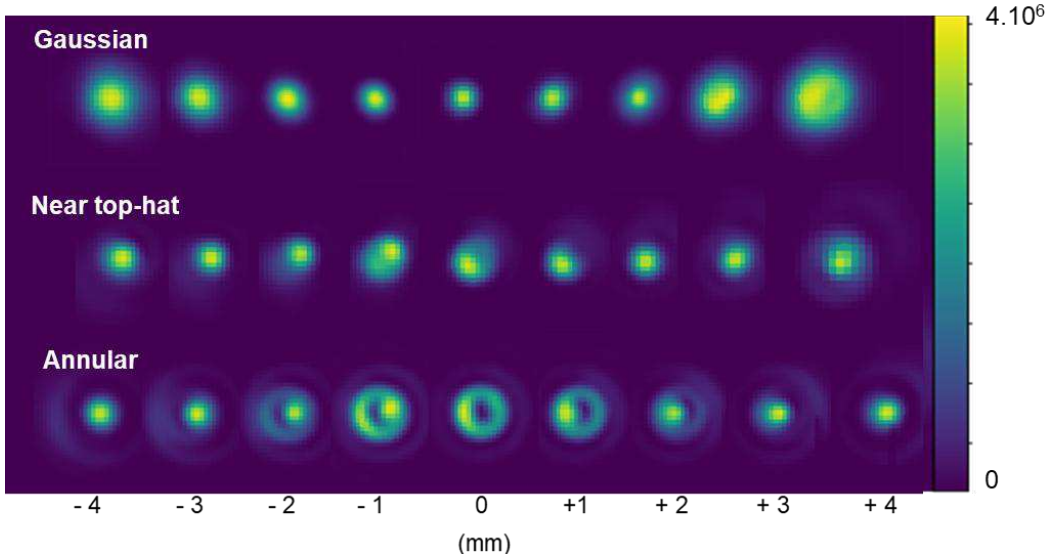


Fig. 1: *Beam analysis of Gaussian, near-top-hat, and annular intensity distributions generated using a diffractive optical element (DOE).*

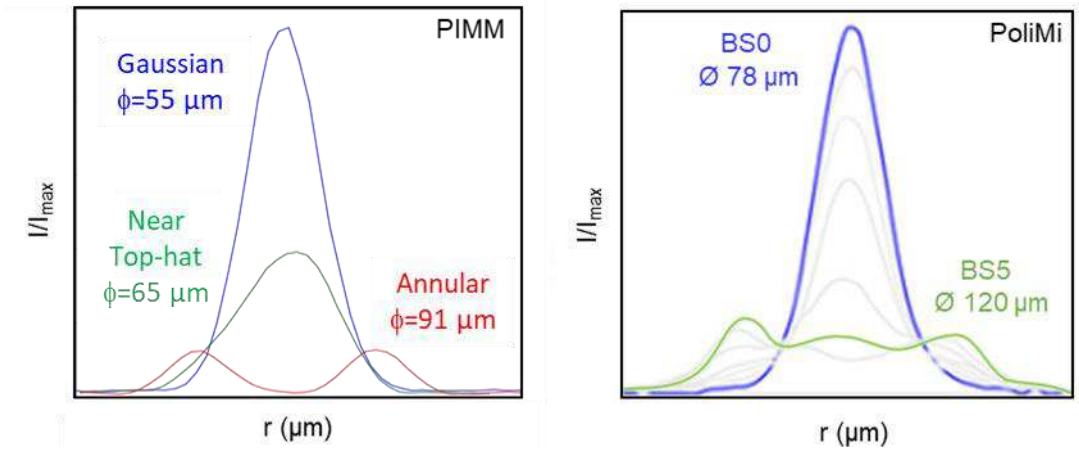


Fig. 2: *Measured laser-intensity distributions of the beam profiles investigated: (a) DOE-generated profiles used at PIMM; and (b) Gaussian BS0 and near-top-hat BS5 profiles generated using the nLIGHT Corona AFX1000 double-core laser at PoliMi.*

Laser	Beam shaping	Shape	Diameter $D_{4\sigma}$
1 kW red Power QUBE		Gaussian	55
1 kW red Power QUBE	DOE	Near-top-hat	65
1 kW red Power QUBE	DOE	Annular	91
1 kW nLIGHT AFX1000	Double core	Gaussian (BS0)	70
1 kW nLIGHT AFX1000	Double core	Near-top-hat (BS5)	200

Table 1*: Laser systems, beam-shaping methods, beam-profile configurations, and corresponding measured $D_{4\sigma}$ spot diameters used in the PIMM and PoliMi experiments.*

	Beam shaping	Specimen dimensions (mm^3)	Laser power (W)	Scan speed ($m.s^{-1}$)	Hatch distance (µm)
PIMM	DOEs	10 x 10 x 2	150 to 900	0.5 to 3.2	150
PoliMi	Double core	11 x 11 x 11	350	0.5 to 1.6	50, 150

***Table 2**: Specimen dimensions and L-PBF processing parameters investigated at PIMM and PoliMi.*

2.3. Characterization of the as-built material

2.3.1. Surface topography

The top surfaces of the specimens were characterized over an area of 4 × 4 mm² using a Bruker InfiniteFocus SL optical profilometer. These measurements were used to assess process stability by identifying surface defects and spatial variations in the build height.

2.3.2. Metallographic preparation

Cross-sections were extracted perpendicular to the final-layer scan direction and prepared using a Mecatech 334 SPC polishing system. The specimens were ground using SiC papers with grit sizes of 220, 600, 1000, and 2400, followed by polishing with 3 and 1 µm diamond suspensions. Specimens for EBSD analysis were additionally polished for 30 min using a colloidal silica suspension.

2.3.3. Porosity and relative-density measurements

Porosity was quantified from cross-sectional images covering an area of 6 × 1.5 mm². The images were binarized and analyzed using ImageJ. The area fraction of porosity was calculated as the ratio of the number of pixels corresponding to pores to the total number of pixels within the analyzed 9 mm² cross-sectional area. The relative density was subsequently determined as the complement of the measured porosity fraction.

2.3.4. Melt-track characterization

The polished cross-sections were chemically etched using Keller's reagent, consisting of 1 mL HF, 2 mL HCl, 3 mL HNO_3, and 95 mL H_2O. Melt-track boundaries were then examined using a ZEISS Axio Imager M2m optical microscope.

2.3.5. EBSD characterization

EBSD measurements were performed using ZEISS EVO and ZEISS LEO Gemini 1530 scanning electron microscopes operated at an accelerating voltage of 20 kV and a probe current of 10 nA. A step size of 1 µm was used. Data acquisition, indexing, and post-processing were performed using NORDIF and OIM Data Collection software. Crystallographic textures were evaluated using the harmonic method with a series-expansion order of (L = 30). Individual orientations were represented using Gaussian functions with a half-width of 5°.

2.3.6. Tensile testing

Flat tensile specimens, 6 mm wide and 1.5 mm thick, with a gauge length of 40 mm, were built vertically, parallel to the build direction, and tested at room temperature using an Instron 5581 universal testing machine. A nominal strain rate of 5×10^{-4} s^{-1} was applied. Before testing, approximately 200 µm of material was removed from the specimen surfaces by mechanical

polishing to reduce the influence of as-built surface roughness. Strain was measured using an Instron 2630-101 extensometer with a gauge length of 10 mm.

3- Results and discussion

3.1. Influence of laser beam shaping on melt-pool geometry and L-PBF process stability

3.1.1. Melt-pool dimensions

Melt-pool dimensions were measured on micrographic cross-sections of specimens manufactured at PIMM. The mean width, (w), and penetration depth, (e), were determined from six adjacent tracks in the final deposited layer (**Fig. 3**).

Beam shaping markedly reduced the melt-pool penetration depth, particularly under annular irradiation. The maximum depth did not exceed 200 µm with the annular beam, compared with approximately 330 µm for the near-top-hat beam and up to 500 µm for the Gaussian beam. Smaller differences were observed in melt-pool width. Nevertheless, the annular beam also produced slightly narrower melt pools, with a maximum width of approximately 320 µm, compared with approximately 400 µm for the near-top-hat and Gaussian beams. Consequently, for a given (P/V) ratio, i.e., a given combination of laser power and scan speed, the annular and near-top-hat beams produced lower depth-to-width ratios than the Gaussian beam. The measured ranges were ($0.45 < e/w < 0.60$) for the annular beam, ($0.50 < e/w < 0.90$) for the near-top-hat beam, and ($0.60 < e/w < 1.20$) for the Gaussian beam. Thus, beam shaping produced shallower melt pools with flatter boundaries.

Following the analytical approaches proposed in [27] and [28], the normalized melt-pool penetration depth, expressed as the ratio ($e/D_{4\sigma}$), was plotted as a function of volumetric energy density ($J.mm^{-3}$), considered as P/(V.S), where *S* is the laser spot area (mm^2) (**Fig. 4**). This representation indicates a transition in the melting regime at approximately 70-80 $J.mm^{-3}$. Below approximately 70 $J.mm^{-3}$, the $e/D_{4\sigma}$ ratio increases gradually from approximately 0.9 to 1.5, consistently with a predominantly conduction-controlled regime. Above approximately 80 $J.mm^{-3}$, the pronounced increase in slope indicates the onset of keyhole-mode melting. As a reminder, the keyhole threshold is usually considered as $e/D \approx 1$, corresponding approximately to a 45° inclination of the liquid–vapor interface induced by recoil pressure. At steeper inclination angles, multiple reflections of the incident laser beam within the vapor depression enhance energy deposition at the melt-pool bottom, thereby promoting vapor-capillary formation. In aluminium alloys, the high thermal diffusivity may shift this transition to larger ($e/D_{4\sigma}$) values, potentially approaching 1.5, as suggested by the present observations.

Melt-pool dimensions were also measured on specimens manufactured at PoliMi using the BS0 (gaussian) and BS5 (near-top-hat) profiles at a laser power of 350 W (**Table 1**). The corresponding data are highlighted in red in **Fig. 3** and **Fig. 4**. For comparable beam profiles, the double-core laser used at PoliMi produced variations in melt-pool depth and width similar to those obtained at PIMM using diffractive optical elements (DOEs), despite its larger beam diameters. The two systems therefore show the same qualitative effect of irradiance redistribution on melt-pool geometry.

The lower penetration obtained with the near-top-hat and annular profiles can mainly be attributed to their lower peak irradiance. With the Gaussian profile, the concentration of energy near the beam axis promotes evaporation and recoil pressure, leading to a deeper surface depression and eventually to keyhole formation [3]. Redistributing power away from the beam

centre primarily reduces penetration, while having a smaller effect on melt-pool width. This is consistent with the lower depth-to-width ratios measured for the shaped profiles, particularly the annular beam. Similar effects of core-to-ring power redistribution on melt-pool geometry have been reported by [17] and [22]. In the PIMM experiments, these differences were observed with beam diameters close to those conventionally used in L-PBF, suggesting that they arise from the irradiance distribution and not solely from the large spot sizes considered in many previous beam-shaping studies.

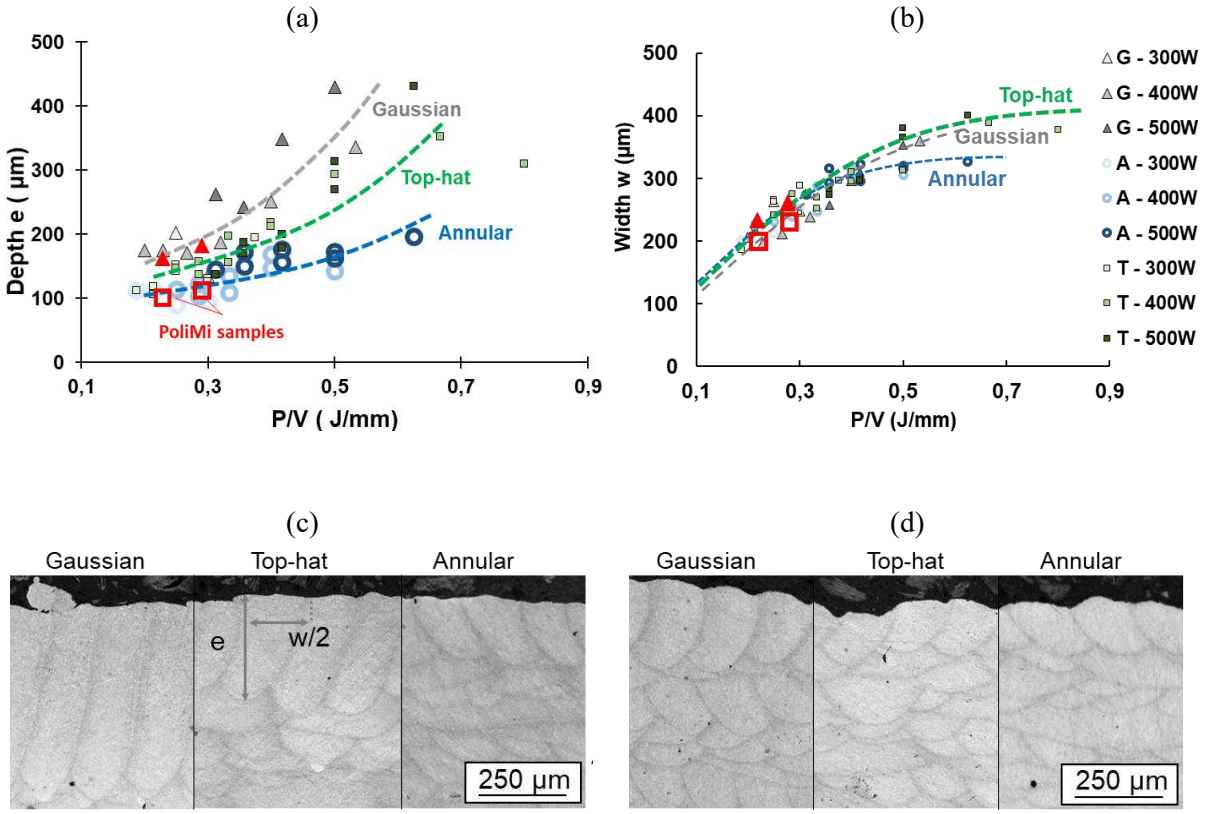


Fig. 3: *Melt-pool dimensions and cross-sectional morphologies of L-PBF tracks measured in the final deposited layer: (a) penetration depth and (b) width. Red symbols denote specimens fabricated at PoliMi at 350 W and scan speeds of 1.2 m.s^{-1} (triangle) and 1.6 m.s^{-1} (square). Representative cross-sections obtained at 500 W and scan speeds of (c) V = 1 m.s^{-1} and (d) V =1.6 m.s^{-1}.*

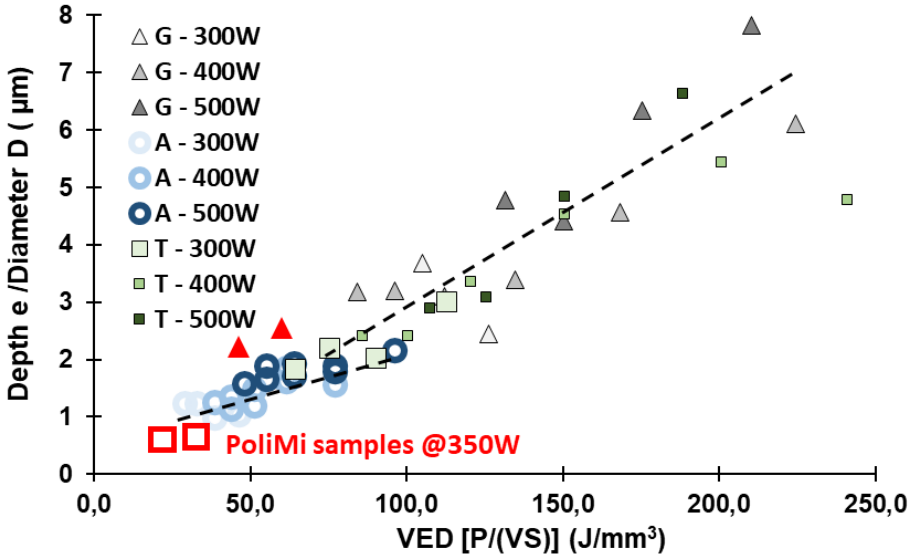


Fig. 4: *Normalized melt-pool penetration depth, e/D, as a function of volumetric energy density for the Gaussian (G), near-top-hat (T), and annular (A) beam profiles. The gradual increase in e/D below 70 J.mm^{-3} is characteristic of conduction-controlled melting, whereas the marked increase above 80 J.mm^{-3} indicates the onset of keyhole-mode melting. Data obtained at PoliMi for specimens fabricated at 350 W and scan speeds of 1.2 m.s^{-1} (triangle) and 1.6 m.s^{-1} (square) are shown in red.*

3.1.2. Process stability

The stability of the L-PBF process under various beam-shaping conditions was assessed using the MiMAS PIMM setup through a combination of post-mortem and real-time analyses: (i) construction of single-track stability maps in the (P, V) parameter space, (ii) high-speed imaging of spatter generation during L-PBF, and (iii) evaluation of the surface finish of the top surfaces of rectangular specimens.

First, single tracks were deposited on a pre-built L-PBF surface, with the scanning direction rotated by 90° relative to that of the underlying layer, to reproduce conditions representative of contour scanning (**Fig. 5**). Track continuity was used as a key indicator of process stability. Lateral instabilities and vertical humping may impair the overlap between adjacent tracks, thereby promoting the formation of lack-of-fusion defects. The results show that the annular beam shape extends the stable processing window (shown in green) toward higher laser powers (up to 900 W in the present study) and higher scan speeds compared with the G and T beam shapes. However, within the laser-power range typically used for aluminum alloys (300–400 W), track discontinuities occur at lower scan speeds with T and A beam shapes, due to insufficient volumetric energy density. These findings suggest that, provided sufficient laser power is available, the annular beam profile may enable processing at higher scan speeds.

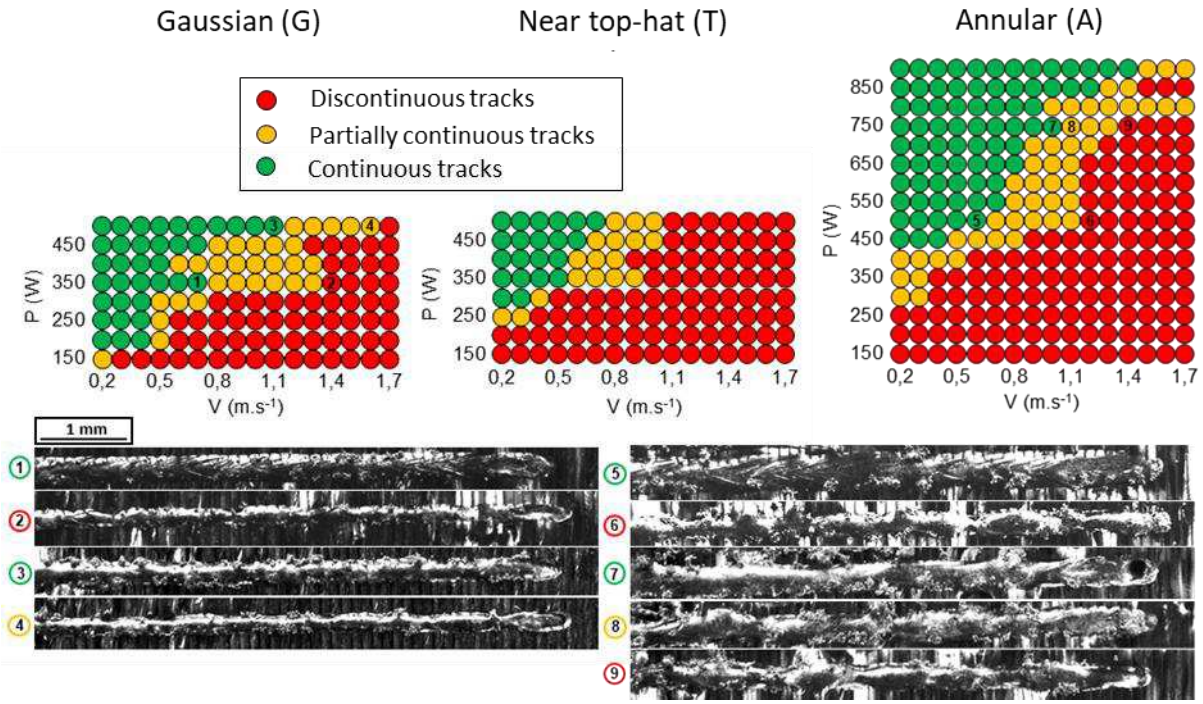


Fig. 5: *Laser power–scan speed (P,V) stability maps for single tracks deposited on a pre-built L-PBF surface using Gaussian, near-top-hat, and annular beam profiles. Green denotes stable and regular tracks, orange partially discontinuous tracks, and red discontinuous tracks.*

The number and size of the spatters generated during L-PBF were examined as additional indicators of process stability. Several mechanisms may contribute to spatter formation [7], including:

- Friction between the melt pool and the vapor flow near the laser-matter interaction zone;
- Acceleration of the melt flow to velocities at which inertial forces overcome surface tension, promoting the ejection of large spatter particles;
- Direct entrainment of powder particles from the denuded zone by the expanding vapor plume.

Side-view high-speed imaging at 10 kfps was used to quantify the bright, high-temperature spatters. The three beam profiles were compared at a constant laser power of 450 W and a scan speed of 1.2 m s^{-1}. Surprisingly, ***Fig. 6*** reveals that both the number and relative size of the spatters were greater under annular (A) and near-top-hat (T) irradiation than under Gaussian (G) irradiation, with increases of up to a factor of five for the A beam. Given that the A beam produced a smaller melt-pool volume under identical (P) and (V) conditions (**Fig. 3a and b**), these results suggest that the ratio of ejected material to consolidated material increased markedly under A irradiation and, to a lesser extent, under T irradiation. Furthermore, the vapor plume appeared progressively more pronounced with the annular beam shape (***Fig. 6a***). This behavior is counterintuitive, considering the lower maximum intensity associated with the A beam profile (**Fig. 2**). These findings also suggest that the transition from a deep keyhole mode (G) to a near-conduction mode (A) does not necessarily stabilize the spatter generation. The physical mechanism responsible for this behavior remains unclear.

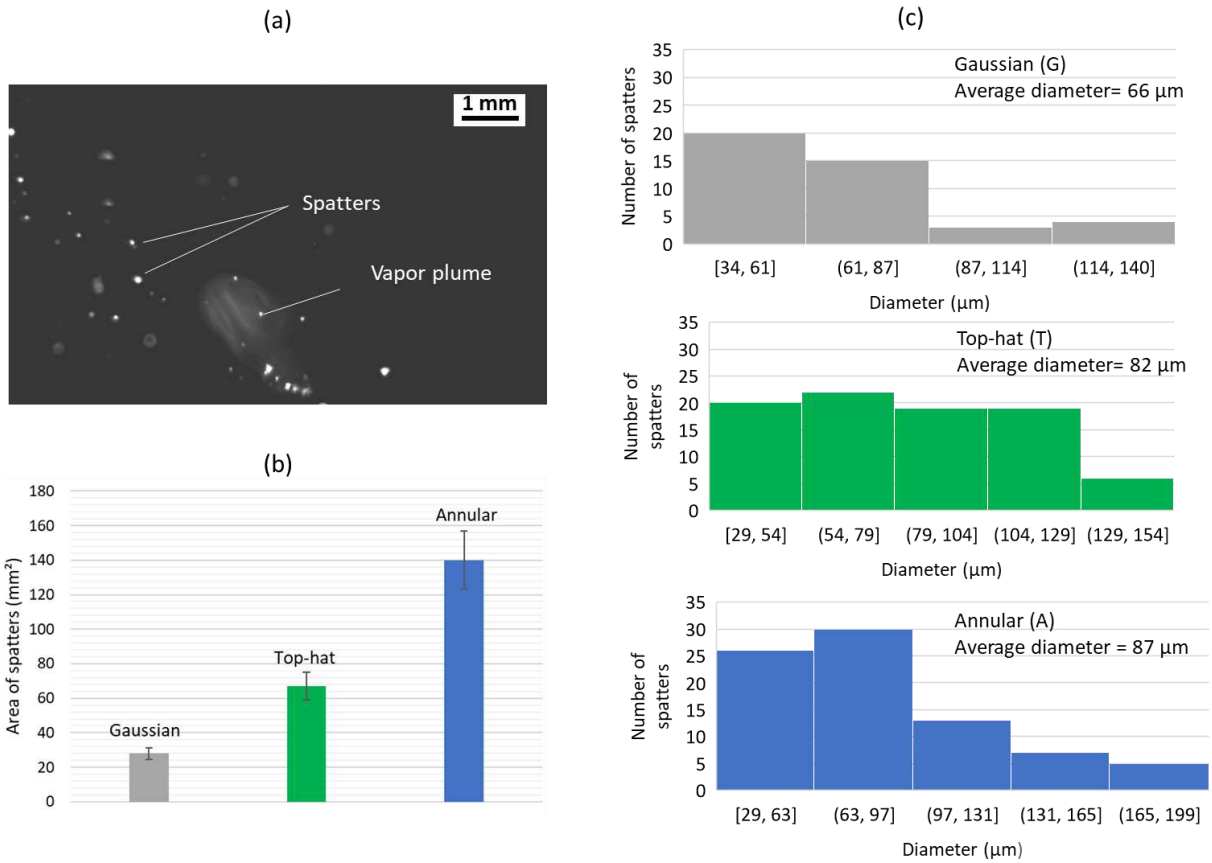


Fig. 6: *High-speed imaging analysis of spatter emission at 10,000 fps for P = 450 W, V = 1.2 m.s^{-1} :(a) Example of captured image, (b) Total projected spatter area detected over seven L-PBF tracks, (c) equivalent spatter diameter.*

The morphology of the top build surface reflects several physical phenomena, including vertical melt-pool oscillations, the effectiveness of track overlap, and the amount and size of redeposited spatter. Specimens were manufactured at 500 W using scan speeds of 1.0 and 1.6 m s^{-1}, corresponding to (P/V) ratios of 0.50 and 0.31 J.mm^{-1}, respectively. The surfaces shown in **Fig. 7** correspond to the condition (P = 500 W and V = 1.6 m s^{-1}). They clearly demonstrate the smoothing effect of the near-top-hat and annular profiles. Regardless of the surface parameter considered (Sa, Sv, or Sdr), beam shaping produced smoother top surfaces despite the increased spatter emission observed in **Fig. 6**. This improvement can be associated with the shallower and more conduction-dominated melt pools produced by the shaped beams at 500 W.

Overall, aside from the increased spatter emission, the use of DOEs stabilized the melt pools under comparable laser power and scanning-speed conditions. The annular profile was particularly effective in producing continuous tracks and smooth build surfaces. Improved top-surface quality is expected to promote uniform deposition of subsequent powder layers, thereby minimizing localized variations in powder-bed thickness and mitigating the risk of lack-of-fusion defects.

Although the shaped beams generated more spatter, the resulting surfaces remained smoother. This suggests that spatter emission alone does not fully reflect process stability. Melt flow, vapour expansion, and powder entrainment may all contribute to spatter formation [6, 7]. Synchronized imaging could help clarify their respective roles, while powder-spreading tests would show whether the smoother surfaces improve the uniformity of subsequent layers.

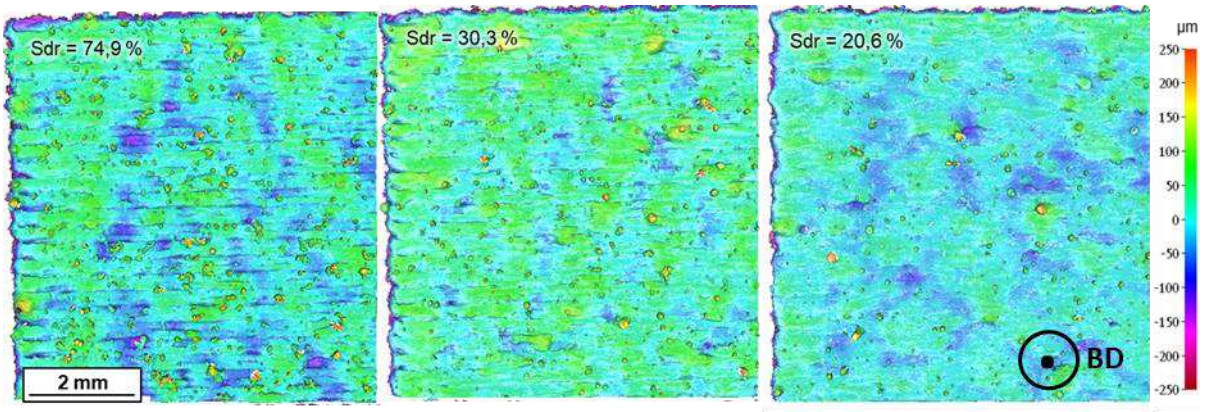


Fig. 7: *3D top-surface profiles of specimens manufactured at P=500 W and V= 1.6 m.s^{-1} using Gaussian (G, left), near-top-hat (T, center) and annular (A, right) beam profiles.*

(a) (b)

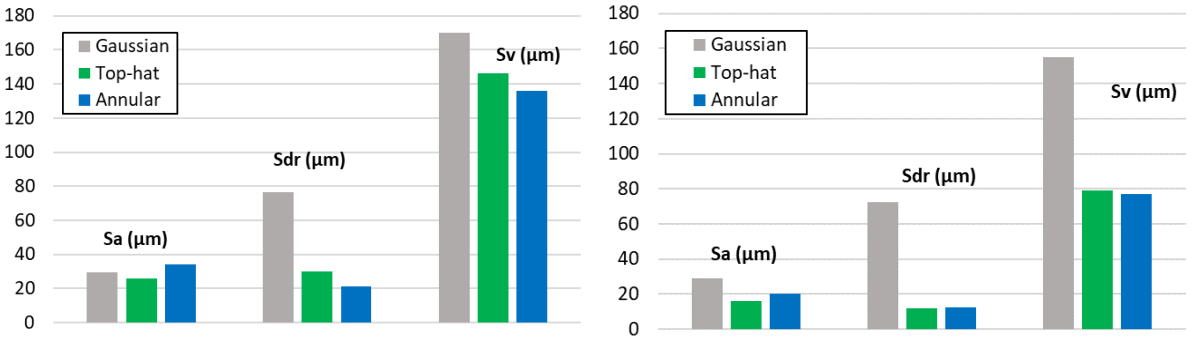


Fig. 8: *Surface roughness parameters measured on the as-built surfaces for two processing conditions: (a) 500 W – 1.6 m.s^{-1}, (b) 500 W – 1 m.s^{-1}. The parameters shown are the arithmetical mean height (Sa), maximum pit height (Sv), and developed interfacial area ratio (Sdr). Gray, green, and blue represent the Gaussian, near-top-hat, and annular beam profiles, respectively.*

3.2. Influence of beam shaping on density, microstructures, and mechanical properties

3.2.1. Relative density

Fig. 9 shows cross-sections of specimens fabricated at a constant laser power of 500 W, across four scan speeds (1.0, 1.2, 1.4, and 1.6 m.s^{-1}), and three DOE-generated beam profiles: Gaussian (G), near-top-hat (T), and Annular (A). Nearly spherical pores associated with keyhole instability are observed in all specimens produced with the Gaussian profile. By contrast, no such pores were observed in the near-top-hat specimens produced at scan speeds above 1.2 m.s^{-1} or in any of the specimens produced with the annular profile. These findings indicate that, under Gaussian irradiation at 500 W, increasing the scan speed over the investigated range did not eliminate keyhole porosity. Conversely, the broader distribution of laser energy provided by the near-top-hat and annular profiles enabled higher scan speeds without detectable keyhole porosity. Further increasing the scan speed could mitigate keyholing with the Gaussian profile, but would require a smaller hatch spacing to maintain track overlap and prevent lack-of-fusion

defects.
Another effect of beam shaping is illustrated in
Fig. 10. The optimum P/V processing window is remarkably narrow for Gaussian (G) irradiation (0.25 to 0.38 J.mm^{-1}) but significantly broader for the near-top-hat (T) and annular (A) profiles. Above approximately 0.4 J.mm^{-1}, keyholing becomes dominant in the G specimens and, to a lesser extent, in the T specimens, whereas the A specimens maintain a high density level exceeding 99.5%. Although all three beam shapes achieve the same maximum density (> 99.9%), optimum densification requires higher laser powers for the T (450–500 W) and A (500 W) configurations than for the initial G profile (350–400 W). Corresponding optimal VED (J.mm^{-3}) ranges are as follows: [50-100] for the A beam, [80-140] for the T beam, and [100-150] for the initial G beam. The wider processing window obtained with the shaped beams is attributed to their lower peak irradiance, which delays excessive penetration and keyhole formation. A similar trend was reported for annular irradiation by [15].
A second batch of specimens was manufactured at PoliMi using BS0 (Gaussian) and BS5 (near-top-hat) beam profiles at a constant laser power of 350 W and two hatch spacings (50 µm and 150 µm) (**Fig. 11**). A relative density exceeding 99.7% was achieved with the larger hatch distance (150 µm), performing similarly to the DOEs. Reducing the hatch spacing to 50 µm induced greater scattering and globally decreased the density values, regardless of the beam shape.

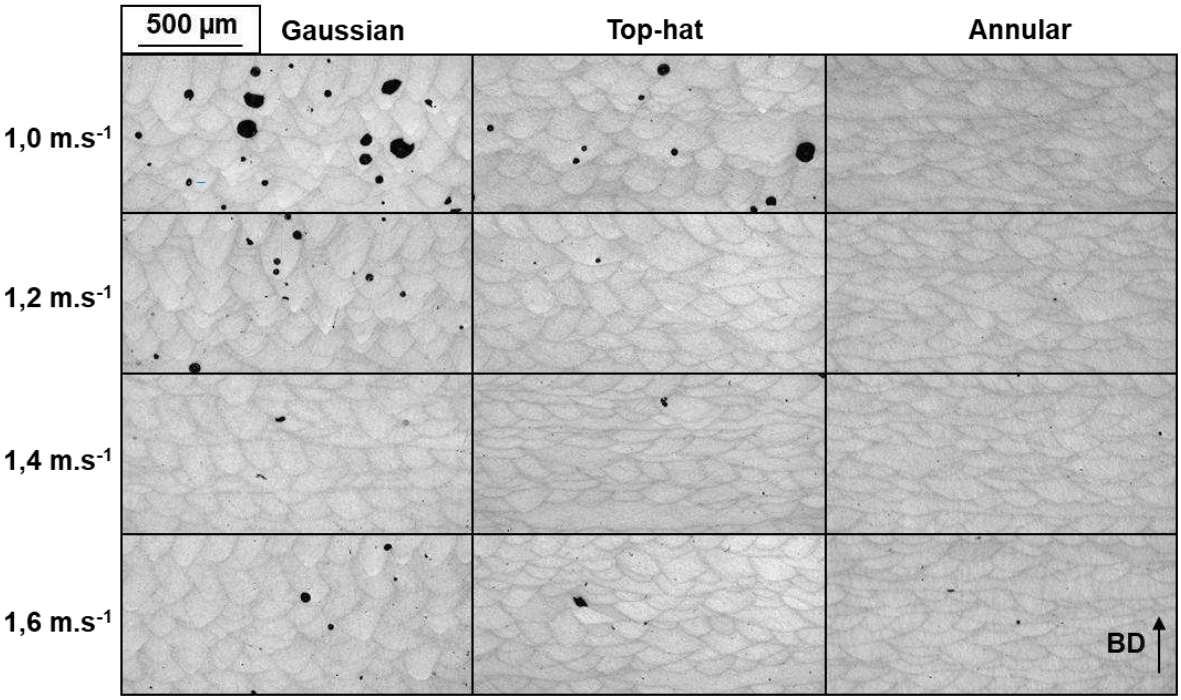


Fig. 9: *Optical micrographs of cross-sections from specimens manufactured at P = 500 W using Gaussian, near-top-hat, and annular beam profiles at different scan speeds. The hatch spacing was 150 µm.*

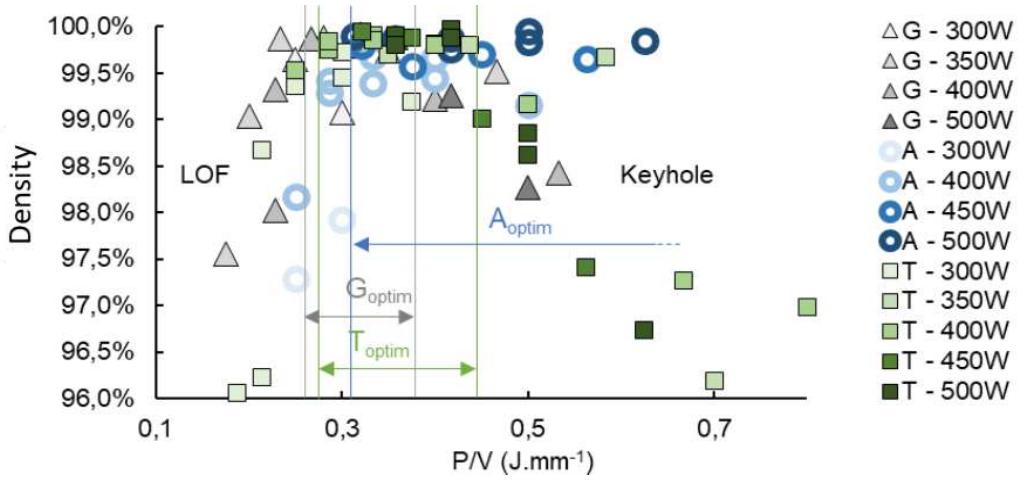


Fig. 10: *Density of specimens manufactured using the Gaussian (G), near-top-hat (T) and Annular (A) beam shapes generated by DOEs. Laser powers ranging from 300 W to 500 W were investigated at a hatch spacing of 150 µm. Gray, green, and blue denote the Gaussian, near-top-hat, and annular profiles, respectively.*

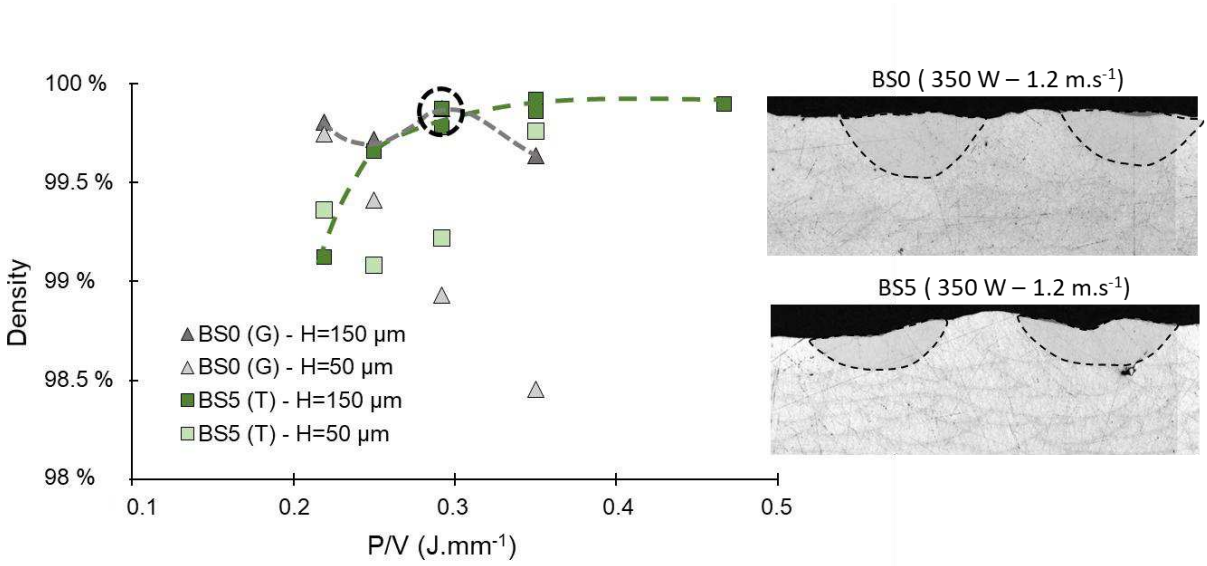


Fig. 11: *Density of specimens manufactured using the BS0 (G) and BS5 (T) beam shapes generated by the double-core laser at P = 350 W and hatch spacings of 50 and 150 µm. Representative melt-pool geometries obtained with BS0 and BS5 at P/V = 0.29 J.mm^{-1} (350 W and 1.2 m.s^{-1}) are also shown.*

3.2.2. Microstructure and crystallographic texture

Electron backscatter diffraction (EBSD) was used to analyze the grain morphology, crystallographic orientation, and size distribution of specimens fabricated using various beam profiles. **Fig. 12** displays cross-sectional inverse pole figure maps along the build direction (IPF-Z) with the corresponding pole figures, for specimens processed at 350 W and 1.2 m.s^{-1} using Gaussian (G), near-top-Hat (T), and Annular (A) diffractive optical elements (DOEs). All three specimens exhibit a strong, predominant <001> fiber texture, characteristic of the 67° interlayer rotation strategy. The texture intensity (TI) increases from 2.02 for the G beam profile to 2.79 and 2.92 for the T and A beam profiles, respectively. Nevertheless, these values indicate

relatively weak textures compared with those typically reported for strongly oriented L-PBF microstructures. The differences in grain size among the three conditions remain limited, although slightly larger equivalent grain diameters are observed for the near-top-hat and annular profiles.

In the IPF maps, regions corresponding to grains with a <001> orientation parallel to the build direction (BD) are preferentially located near the melt-pool bottoms. At these locations, the local thermal gradient, and therefore the preferred solidification direction, is approximately parallel to the BD. Beam shaping slightly increases the area fraction of these regions from 7% to 9%, making this orientation highly dominant over the <011> and <111> orientations (**Fig. 13**). For the specimen produced with the annular profile, the <001> pole exhibits a broader angular distribution. Thus, despite the higher area fraction of <001>-oriented regions, their orientations are more widely distributed around the ideal <001>//(BD) orientation (**Fig. 12**).

The increase in texture intensity induced by beam shaping may be attributed to changes in melt-pool geometry. The melt-pool width-to-depth ratio increased from approximately 1.4 under Gaussian irradiation to 2.1 under annular irradiation, while the near-top-hat and annular profiles produced flatter melt-pool bottoms. This geometry increases the proportion of the melt-pool boundary oriented nearly perpendicular to the build direction (BD), thereby promoting epitaxial growth along the BD. In face-centered cubic alloys, the preferred <001> solidification direction tends to align with the maximum local thermal gradient, which is approximately normal to the melt-pool boundary. At a hatch spacing of 150 µm, the overlap between adjacent tracks increased from approximately 40% for the Gaussian profile to 45% and 52% for the near-top-hat and annular profiles, respectively. The overlap between adjacent tracks was calculated as $O = ((w-h)/w) \times 100$ where w is the melt-pool width and h is the hatch spacing. The correlation between greater track overlap and stronger crystallographic texture is qualitatively consistent with the observations reported previously [29] for nickel-based alloys processed by L-PBF.

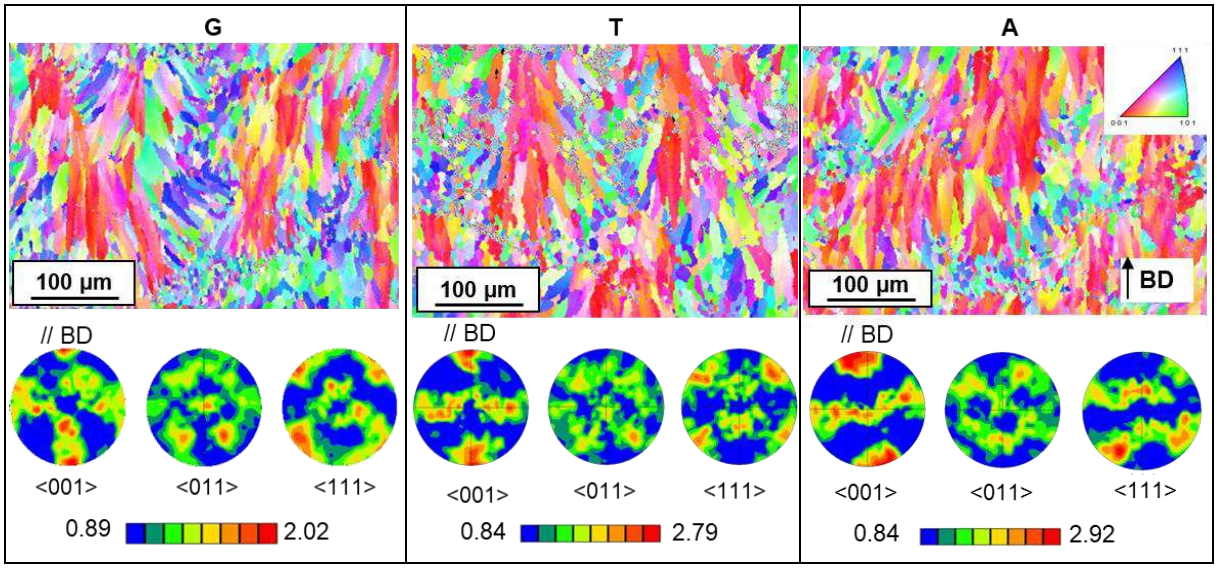


Fig. 12: *EBSD characterization of specimens manufactured at PIMM using Gaussian (G), near-top-hat (T), and annular (A) beam profiles at P = 350 W, V = 1.2 m.s^{-1} and a hatch spacing of 150 µm: inverse pole figure maps along the build direction (IPF-BD) and corresponding pole figures.*

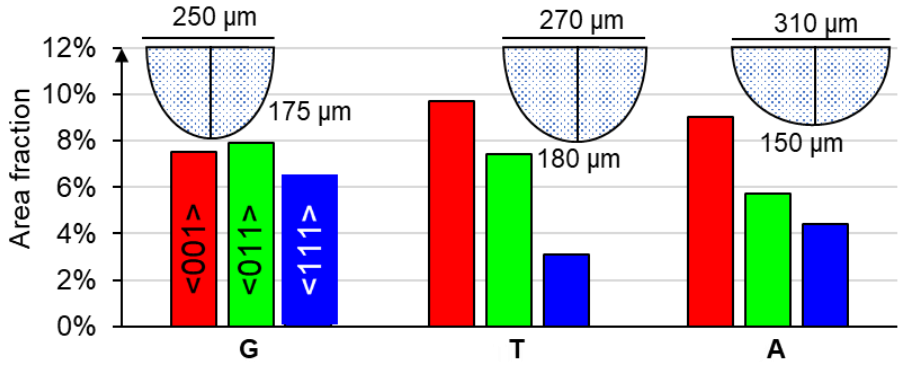


Fig. 13: *Area fractions of grains oriented close to the <001>, <011>, and <111> directions in specimens manufactured at PIMM using Gaussian, near-top-hat, and annular beam shapes at P = 350 W, V = 1.2 m.s^{-1}, and a hatch spacing of 150 µm. The corresponding influence of melt-pool morphology is also shown.*

EBSD analyses conducted over larger (700 × 700 µm^2) fields of view on specimens fabricated using the dual-core laser with the BS0 (Gaussian, G) and BS5 (near-top-hat, T) beam profiles confirm the trends observed with the diffractive optical elements (DOEs). All specimens exhibit a pronounced <001> // BD fiber texture, with comparable texture intensities for the two beam-shaping approaches. For example, the BS5 profile with a hatch spacing of 150 µm yields a texture index of 2.62 at a scan speed of 1.4 m.s^{-1} (**Fig. 14a**), compared with 2.79 for the DOE-generated near-top-hat profile at 1.2 m.s^{-1}. The corresponding area fractions of <001> grains are also comparable (**Fig. 15**), and no appreciable differences in grain size are observed between the two processing approaches. These observations demonstrate that the principal microstructural trends obtained using the static DOEs can be reproduced using dynamic double-core beam shaping.

Further insight into the effect of track overlap on microstructural evolution was obtained by reducing the hatch spacing from 150 to 50 µm. The resulting increase in overlap strengthened the <001> // (BD) texture. At a scan speed of 1.4 m.s^{-1}, the texture index reached 3.13 for the BS0 Gaussian (G) beam profile (**Fig. 14b**) and 4.18 for the BS5 near-top-hat (T) profile (**Fig. 14c**). The fraction of <001> oriented grains also increased, reaching approximately 15% for the BS5 specimen manufactured using a hatch spacing of 50 µm (**Fig. 15**). The elongated grains also exhibited a more pronounced alignment with the build direction, particularly for the BS5 profile (**Fig. 14c**). These results indicate that combining beam shaping with increased track overlap promotes texture development and, consequently, greater crystallographic anisotropy.

At a scan speed of 1.2 m.s^{-1}, matching that used for the DOE-fabricated specimens, the combination of the BS5 profile and a hatch spacing of 50 µm produced the strongest texture, with a texture index of 5.29 and an area fraction of <001>-oriented grains of approximately 19% (Fig. 14d and **Fig. 15**).

Consistent with the strengthening of the <001>//BD texture, reducing the hatch spacing from 150 to 50 µm decreased the mean Taylor factor, (M), from approximately 2.85 to 2.72. By comparison, the influence of beam shape was modest: switching from the Gaussian to the near-top-hat profile reduced (M) by only approximately 0.02.

Beam shaping had a greater effect on crystallographic texture than on grain size. This differs from the grain coarsening reported for substantially larger Gaussian beams [18], suggesting that texture can be modified without substantial grain growth. Track overlap had a stronger influence on texture than the beam profile alone. Moreover, the broader <001> pole distribution obtained with the annular profile shows that a larger <001> fraction does not necessarily correspond to a more sharply defined fiber texture.

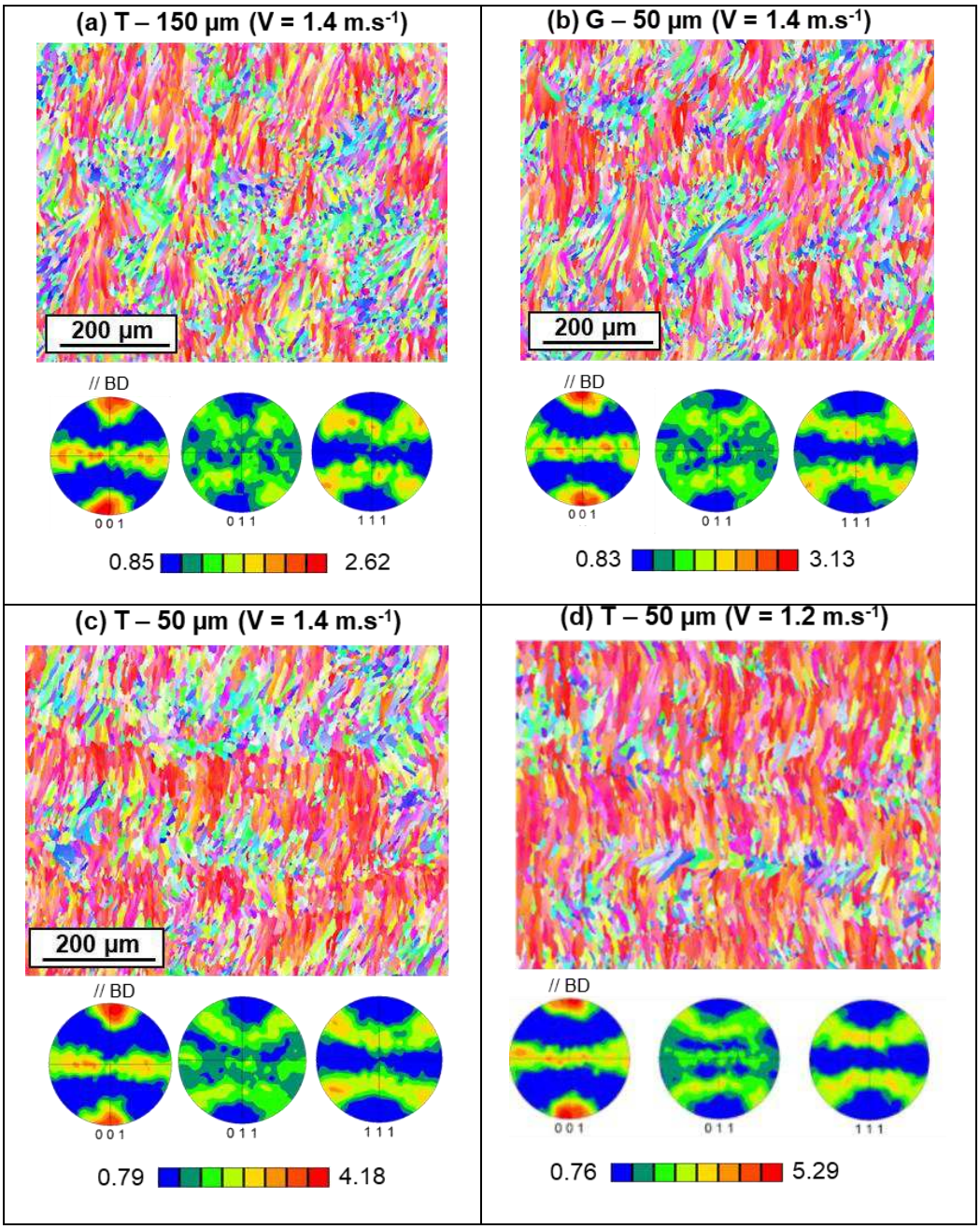


Fig. 14: *EBSD characterization of specimens manufactured at PoliMi at P = 350 W using (b) the BS0 Gaussian profile and (a, c, d) the BS5 near-top-hat profile, with hatch spacings of 50 or 150 µm: inverse pole figure maps along the build direction (IPF-BD) and corresponding pole figures. The scan speed was 1.4 m.s^{-1} in (a–c) and 1.2 m.s^{-1} in (d).*

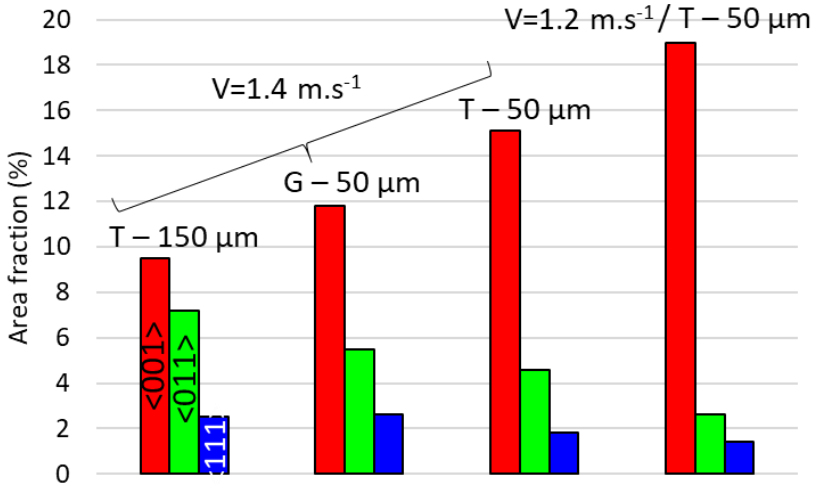


Fig. 15: *Area fractions of grains oriented close to the <001>, <011>, and <111> directions in specimens manufactured using the double-core laser at P = 350 W with the BS0 Gaussian and BS5 near-top-hat profiles. The effects of hatch spacing and scan speed are shown.*

3.2.3. Mechanical properties

Tensile tests were conducted on vertically built specimens manufactured using the double-core laser at PoliMi. The BS0 Gaussian and BS5 near-top-hat profiles were compared at a constant laser power of 350 W, scan speeds of 1.2 and 1.4 $m.s^{-1}$, and hatch spacings of 50 and 150 µm. Two specimens were tested for each processing condition, and the resulting mechanical properties are summarized in **Fig.16**.

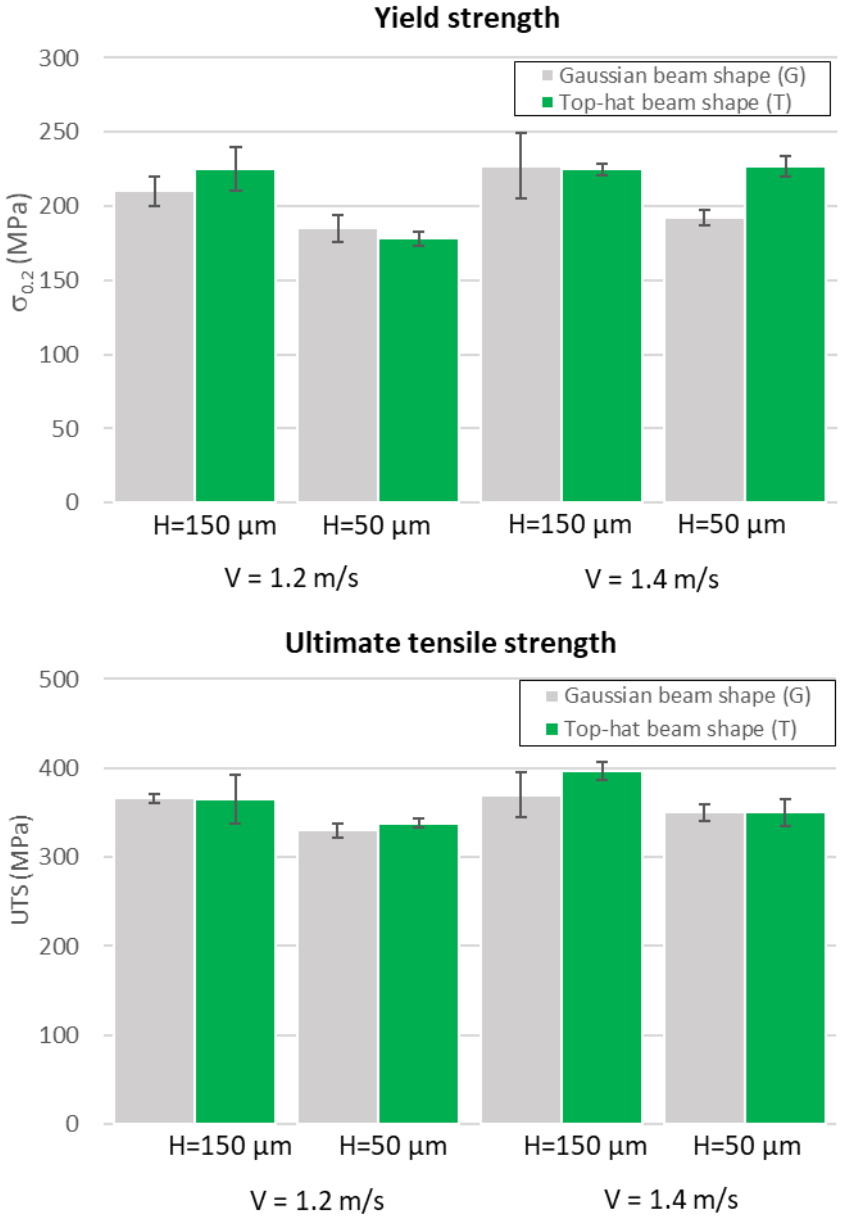
For comparable laser power and scanning-speed conditions, beam shaping had a moderate overall effect on the tensile properties. The highest ultimate tensile strength UTS (397MPa) was obtained using the near-top-hat profile at V = 1.4 $m.s^{-1}$ and H = 150 µm. The largest elongations, approximately 5%, were obtained using the near-top-hat profile and the smaller hatch spacing. Across all conditions, the mean yield strength, UTS, and elongation at failure were 208 MPa, 361 MPa, and 4.2%, respectively. These values are slightly lower than those typically reported for as-built AlSi10Mg, despite the comparable relative densities achieved in the present study [18, 30]. This difference may be partly attributed to the vertical orientation of all tensile specimens, for which the loading direction was parallel to the build direction. The elongated grain morphology and cellular structure along the build direction may provide fewer boundaries transverse to the loading axis, thereby reducing strengthening relative to other specimen orientations.

The strengthening of the <001> // (BD) texture reduced the Taylor factor of the near-top-hat specimens and could therefore favor a lower yield strength and greater plastic anisotropy. This trend is consistent with the results for the specimen manufactured using the near-top-hat profile at V = 1.2 $m.s^{-1}$ and H = 50 µm. This specimen exhibited the lowest yield strength (178 MPa), the highest elongation (5.2%), and the strongest <001> //BD texture (**Fig. 14d**).

However, this relationship was not systematic across all conditions. For example, the near-top-hat specimen manufactured at V = 1.4 $m.s^{-1}$ and H = 50 µm also exhibited a pronounced texture (**Fig. 14c**) but did not show a correspondingly low yield strength. The mechanical response

therefore cannot be attributed to crystallographic texture alone and may also depend on porosity, grain and cellular substructure, and local variations in thermal history.

Overall, beam shaping preserved the strength and ductility of the material while improving process stability and widening the processing window. These results show that greater process flexibility can be achieved without compromising tensile performance. Further fracture-surface analysis and tests along different build orientations would help clarify the respective roles of texture, porosity, and local microstructure.



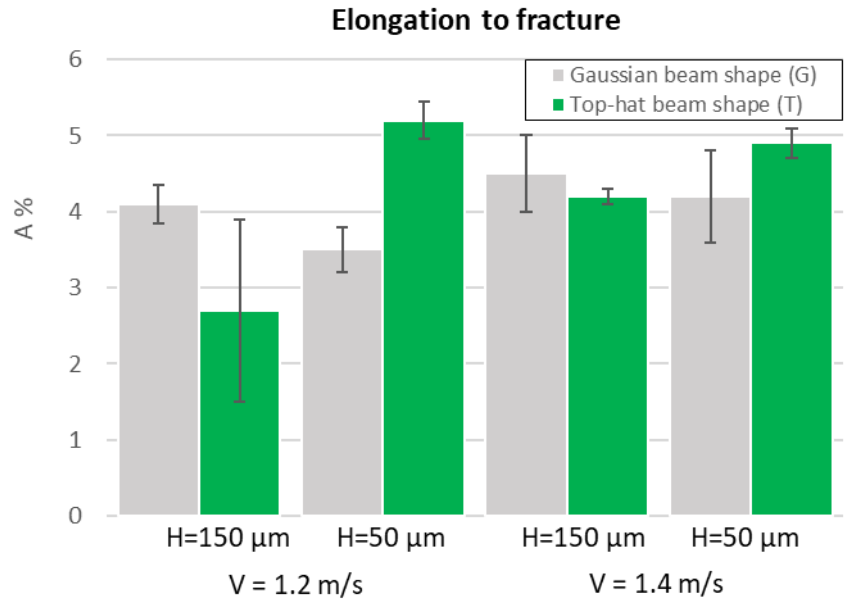


Fig. 16: *Room-temperature tensile properties of specimens manufactured using the BS0 Gaussian (G) and BS5 near-top-hat (T) beam profiles with two scan speeds and two hatch distances.*

3.3. Towards enhanced productivity

At 500 W, the Gaussian beam produced nearly spherical pores associated with keyhole instability across the investigated range of scan speeds, whereas no such pores were detected with the annular profile (**Fig. 9**). The lower peak irradiance of the annular beam therefore appears to accommodate higher laser powers while limiting excessive penetration and keyhole formation.

To assess whether this broader high-power operating range could translate into higher productivity, additional experiments were performed at 700 W using the 90 µm annular beam. Relative densities above 99.5% were maintained at scan speeds of up to 2.6 $m.s^{-1}$ (**Fig. 17**). Beyond this value, lack-of-fusion defects developed and the relative density decreased sharply For comparison, the optimum conditions previously identified for the Gaussian beam were approximately 350 W and 1.4 $m.s^{-1}$ [24]. The annular profile therefore enabled the laser power to be doubled from 350 to 700 W while increasing the maximum scan speed by approximately 85%, from 1.4 to 2.6 $m.s^{-1}$. This result is consistent with the observations of [15], who investigated annular irradiation at laser powers of up to 800 W. The maximum scan speed achieved in the present study, however, was higher than the 2.0 $m.s^{-1}$ reported in that work.

These results highlight a key productivity advantage of beam shaping: higher laser powers can be exploited to increase scan speed and nominal volumetric build rate without inducing severe keyhole instability. The build rate R_b was calculated as $R_b = V \times H \times t$, where V is the scan speed, H the hatch spacing, and t the layer thickness. A maximum build rate of 19.5 $mm^3.s^{-1}$ was achieved using a single laser. Further experiments are needed to determine whether increasing the laser power to 1 kW, combined with a modest increase in hatch spacing, could raise the build rate to 25-30 $mm^3.s^{-1}$. This productivity gain is enabled by the limited variation in melt-pool width and depth with increasing scan speed (**Fig. 18**), consistent with predominantly conduction-controlled heat transfer.

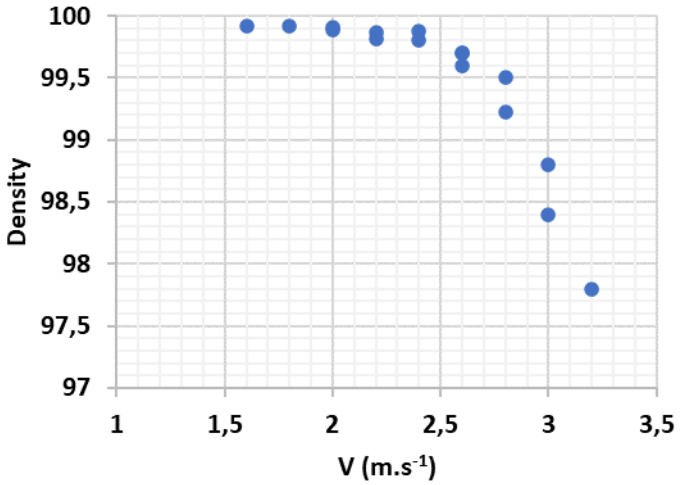


Fig. 17: *Density as a function of scan speed for the annular beam profile at a constant laser power of 700 W and a hatch spacing of 150 µm.*

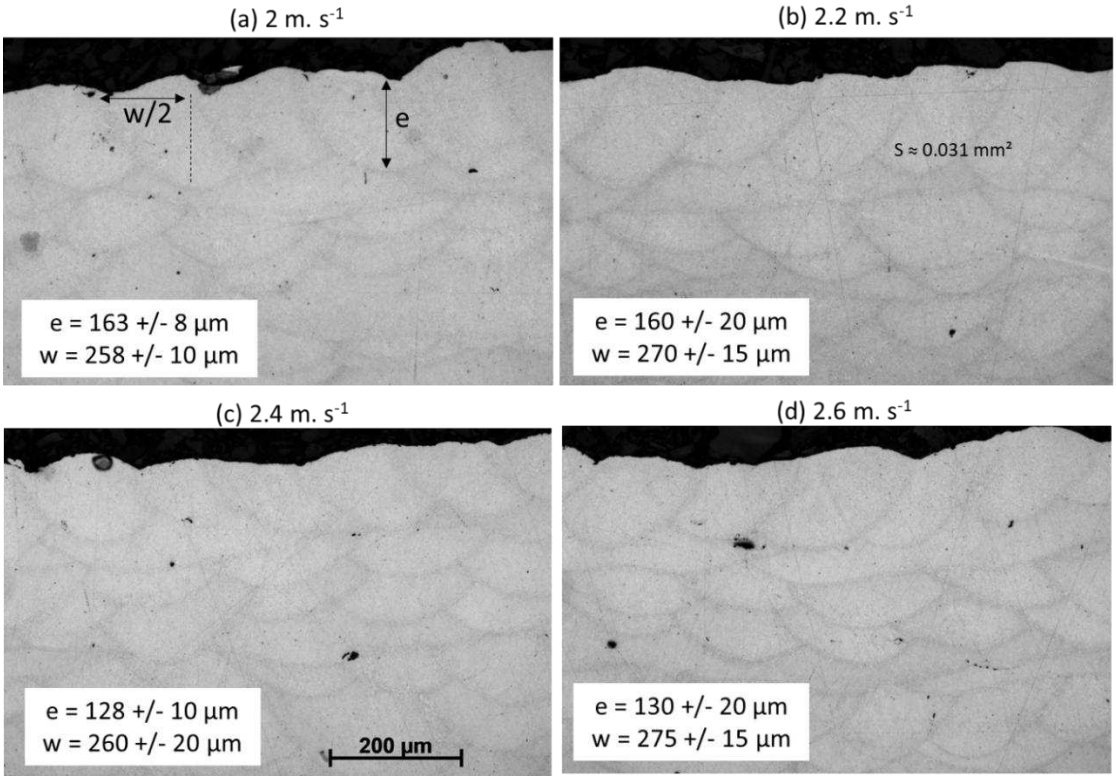


Fig. 18: *Cross-sections of the deposited material, showing the melt pool associated with the final deposited layer, at scan speeds ranging from 2.0 to 2.6 m.s⁻¹, using a 90 µm annular beam at a laser power of 700 W.*

4- Conclusions

The influence of laser beam shaping on process stability, melt-pool dimensions, and resulting microstructures and mechanical strengths of as-built parts was evaluated on an AlSi10Mg aluminium alloy. Two beam-shapes (annular and near-top-hat) obtained with diffractive optical

elements or a dual-core fiber laser were considered, and compared with a conventional Gaussian beam profile.

The results show that small-spot beam shaping can significantly improve the processing flexibility and productivity of L-PBF of AlSi10Mg. By reducing peak irradiance, the near-top-hat and annular profiles produced shallower melt pools, delayed keyhole formation, widened the processing window, and improved top-surface quality compared with the Gaussian reference.

Beam shaping also moderately strengthened the <001> // BD texture without substantially changing grain size. Nearly similar trends were obtained using diffractive optical elements and in-source beam shaping, supporting the transferability of the observed effects, despite the different spot diameters of the shaped beams. Within the investigated conditions, the near-top-hat profile also preserved tensile strength and ductility along build direction (BD) despite the stronger <001>//BD textures. Interestingly, the shaped beams generated more spatter despite producing smoother surfaces, showing that spatter emission alone is not a sufficient indicator of process stability.

The main benefit was obtained with the annular profile at 700 W. Relative densities above 99.5% were maintained up to 2.6 $m.s^{-1}$, corresponding to a build rate of approximately 20 $mm^3.s^{-1}$, an 86% increase compared with the Gaussian reference condition. These results identify small-spot annular beam shaping as a promising route for converting higher laser power into greater productivity while limiting keyhole porosity and maintaining part quality.

Acknowledgements

The authors acknowledge the support of Optoprim, nLIGHT, and Raylase provided for the experiments carried out at Politecnico di Milano.

References

1. King WE, Barth HD, Castillo VM, et al (2014) Observation of keyhole-mode laser melting in laser powder-bed fusion additive manufacturing. Journal of Materials Processing Technology 214:2915–2925. https://doi.org/10.1016/j.jmatprotec.2014.06.005

2. Bitharas I, Parab N, Zhao C, et al (2022) The interplay between vapour, liquid, and solid phases in laser powder bed fusion. Nat Commun 13:2959. https://doi.org/10.1038/s41467-022-30667-z

3. Cunningham R, Zhao C, Parab N, et al (2019) Keyhole threshold and morphology in laser melting revealed by ultrahigh-speed x-ray imaging. Science 363:849–852. https://doi.org/10.1126/science.aav4687

4. Khairallah SA, Anderson AT, Rubenchik A, King WE (2016) Laser powder-bed fusion additive manufacturing: Physics of complex melt flow and formation mechanisms of pores, spatter, and denudation zones. Acta Materialia 108:36–45. https://doi.org/10.1016/j.actamat.2016.02.014

5. Bidare P, Bitharas I, Ward RM, et al (2018) Fluid and particle dynamics in laser powder bed fusion. Acta Materialia 142:107–120. https://doi.org/10.1016/j.actamat.2017.09.051

6. Ly S, Rubenchik AM, Khairallah SA, et al (2017) Metal vapor micro-jet controls material redistribution in laser powder bed fusion additive manufacturing. Sci Rep 7:4085. https://doi.org/10.1038/s41598-017-04237-z

7. Wang D, Wu S, Fu F, et al (2017) Mechanisms and characteristics of spatter generation in SLM processing and its effect on the properties. Materials & Design 117:121–130. https://doi.org/10.1016/j.matdes.2016.12.060

8. Pérez-Ruiz JD, Galbusera F, Caprio L, et al (2024) Laser beam shaping facilitates tailoring the mechanical properties of IN718 during powder bed fusion. Journal of Materials Processing Technology 328:118393. https://doi.org/10.1016/j.jmatprotec.2024.118393

9. Zöller C, Adams NA, Adami S (2024) Beam-shaping in laser-based powder bed fusion of metals: A computational analysis of point-ring intensity profiles. Additive Manufacturing 93:104402. https://doi.org/10.1016/j.addma.2024.104402

10. Roehling TT, Shi R, Khairallah SA, et al (2020) Controlling grain nucleation and morphology by laser beam shaping in metal additive manufacturing. Materials & Design 195:109071. https://doi.org/10.1016/j.matdes.2020.109071

11. Bakhtari AR, Sezer HK, Canyurt OE, et al (2024) A Review on Laser Beam Shaping Application in Laser-Powder Bed Fusion. Adv Eng Mater 26:2302013. https://doi.org/10.1002/adem.202302013

12. Grünewald J, Blickle V, Allenberg-Rabe M, et al (2022) Flexible and highly dynamic beam shaping for Laser-Based Powder Bed Fusion of metals. Procedia CIRP 111:65–70. https://doi.org/10.1016/j.procir.2022.08.124

13. Grünewald J, Gehringer F, Schmöller M, Wudy K (2021) Influence of Ring-Shaped Beam Profiles on Process Stability and Productivity in Laser-Based Powder Bed Fusion of AISI 316L. Metals 11:1989. https://doi.org/10.3390/met11121989

14. Loh LE, Liu ZH, Zhang DQ, et al (2014) Selective Laser Melting of aluminium alloy using a uniform beam profile: The paper analyzes the results of laser scanning in Selective Laser Melting using a uniform laser beam. Virtual and Physical Prototyping 9:11–16. https://doi.org/10.1080/17452759.2013.869608

15. Wischeropp TM, Tarhini H, Emmelmann C (2020) Influence of laser beam profile on the selective laser melting process of AlSi10Mg. Journal of Laser Applications 32:022059. https://doi.org/10.2351/7.0000100

16. Patel S, Chen H, Vlasea M, Zou Y (2022) The influence of beam focus during laser powder bed fusion of a high reflectivity aluminium alloy — AlSi10Mg. Additive Manufacturing 59:103112. https://doi.org/10.1016/j.addma.2022.103112

17. Galbusera F, Caprio L, Previtali B, Demir AG (2023) The influence of novel beam shapes on melt pool shape and mechanical properties of LPBF produced Al-alloy. Journal of Manufacturing Processes 85:1024–1036. https://doi.org/10.1016/j.jmapro.2022.12.007

18. Hung C-H, Chu C-W, Chang T-L, et al (2024) Effect of focal spot size on AlSi10Mg alloy parts fabricated by laser powder bed fusion: Process window, mechanical properties, and microstructure. Journal of Alloys and Compounds 977:173338. https://doi.org/10.1016/j.jallcom.2023.173338

19. Shi R, Khairallah SA, Roehling TT, et al (2020) Microstructural control in metal laser powder bed fusion additive manufacturing using laser beam shaping strategy. Acta Materialia 184:284–305. https://doi.org/10.1016/j.actamat.2019.11.053

20. Jodi DE, Kitashima T, Koizumi Y, et al (2022) Manufacturing single crystals of pure nickel via selective laser melting with a flat-top laser beam. Additive Manufacturing Letters 3:100066. https://doi.org/10.1016/j.addlet.2022.100066

21. Li X, Zhao Y, Peng Y, et al (2025) Bulk single-crystal-like IN738 alloy fabricated using laser powder bed fusion by controlling the thermal flow. Materials Research Letters 13:1072–1079. https://doi.org/10.1080/21663831.2025.2563357

22. Bayat M, Rothfelder R, Schwarzkopf K, et al (2024) Exploring spatial beam shaping in laser powder bed fusion: High-fidelity simulation and in-situ monitoring. Additive Manufacturing 93:104420. https://doi.org/10.1016/j.addma.2024.104420

23. Peyre P, Da Silva JR, Hamouche Z, et al (2024) Size and build strategy effects for the L-PBF process applied to Inconel 625 vertical struts: a combined numerical and experimental approach. Int J Adv Manuf Technol 132:5063–5086. https://doi.org/10.1007/s00170-024-13634-4

24. Hébrard P, Barkia B, Demir AG, et al (2026) Influence of laser pulse frequency and duty cycle on the microstructure and mechanical properties of L-PBF AlSi10Mg. Journal of Materials Research and Technology 43:7190–7208. https://doi.org/10.1016/j.jmrt.2026.07.240

25. Hébrard P, Barkia B, Le Guen E, et al (2026) New insights on the pulsed wave L-PBF process. application to an AlSi10Mg aluminium alloy. Prog Addit Manuf 11:5607–5630. https://doi.org/10.1007/s40964-026-01655-2

26. Galbusera F, Caprio L, Previtali B, Demir AG (2024) Tailoring the microstructure of Fe-2.9wt.%Si alloy in laser powder bed fusion using in-source beam shaping. Optics & Laser Technology 174:110649. https://doi.org/10.1016/j.optlastec.2024.110649

27. Hann DB, Iammi J, Folkes J (2011) A simple methodology for predicting laser-weld properties from material and laser parameters. J Phys D: Appl Phys 44:445401. https://doi.org/10.1088/0022-3727/44/44/445401

28. Fabbro R, Dal M, Peyre P, et al (2018) Analysis and possible estimation of keyhole depths evolution, using laser operating parameters and material properties. Journal of Laser Applications 30:032410. https://doi.org/10.2351/1.5040624

29. Chen J (2022) Single crystalline materials realized by selective laser melting – from process parameters to microstructure evolution. Kassel University

30. Hyer H, Zhou L, Park S, et al (2020) Understanding the Laser Powder Bed Fusion of AlSi10Mg Alloy. Metallogr Microstruct Anal 9:484–502. https://doi.org/10.1007/s13632-020-00659-w

Statements and declarations

Funding. This work was funded by ANR-France (French National Research Agency) in the frame of the NOCOLOX project n°ANR-21-CE08-0048.
Competing interest. The authors have no relevant financial or non-financial interests to disclose.
Contributions. PH and LC carried out LPBF experiments. PH, BB, and PP investigated materials properties. PH, PP and BB wrote the paper. FC and MD participated to the high-speed imaging tests with PH.
PP, AGD, BB, and ELG supervised the work. All partners contributed to the paper proofreading